

PAPER • OPEN ACCESS

Three-dimensional stochastic dynamical modeling for wind farm flow estimation

To cite this article: M V Lingad et al 2024 J. Phys.: Conf. Ser. 2767 052065

View the article online for updates and enhancements.

You may also like

- Measurement of sensitivity level pressure corrections for LS2P laboratory standard microphones
- Lixue Wu, George S K Wong, Peter Hanes et al.
- Impact of volcanic eruptions on extratropical atmospheric circulations: review, revisit and future directions Seungmok Paik, Seung-Ki Min, Seok-Woo Son et al.
- Variational assimilation in combination with a regularization method for sea level pressure retrieval from QuikSCAT scatterometer data II: simulation experiment and actual case study Liang Zhang, , Si-Xun Huang et al.



doi:10.1088/1742-6596/2767/5/052065

Three-dimensional stochastic dynamical modeling for wind farm flow estimation

M V Lingad¹, M Rodrigues¹, S Leonardi¹ and A Zare¹

¹ UTD Wind Energy Center and the Department of Mechanical Engineering, The University of Texas at Dallas, Richardson, TX 75080

E-mail: armin.zare@utdallas.edu

Abstract. Modifying turbine blade pitch, generator torque, and nacelle direction (yaw) are conventional approaches for enhancing energy output and alleviating structural loads. However, the efficacy of such methods is challenged by the lag in adjusting such settings after atmospheric variations are detected. Without reliable short-term wind forecasting tools, current practice, which mostly relies on data collected at or just behind turbines, can result in sub-optimal performance. Data-assimilation strategies can achieve real-time wind forecasting capabilities by correcting model-based predictions of the incoming wind using various field measurements. In this paper, we revisit the development of a class of prior models for real-time estimation via Kalman filtering algorithms that track atmospheric variations using ground-level pressure sensors. This class of models is given by the stochastically forced linearized Navier-Stokes equations around the three-dimensional waked velocity profile defined by a curled wake model. The stochastic input to these models is devised using convex optimization to achieve statistical consistency with high-fidelity large-eddy simulations. We demonstrate the ability of such models in reproducing the second-order statistical signatures of the turbulent velocity field. In support of assimilating ground-level pressure measurements with the predictions of said models, we also highlight the significance of the wall-normal dimension in enhancing two-point correlations of the pressure field between the ground and the computational domain.

1. Introduction

Adjustments to the turbine blade pitch, generator torque, and nacelle direction (yaw) are standard methods for boosting energy production and reducing operation and maintenance costs by mitigating the impact of atmospheric variability on wind plants. In practice, the efficacy of such methods is challenged by the lag in adjusting turbine settings as the operator or control system is informed of varying atmospheric conditions. Short-term wind forecasting tools provide a solution to this issue by estimating the turbulent flow several diameters ahead of wind turbines thereby offering sufficient time for the controller to adjust the turbine settings. To this end, efforts have been made to employ data-assimilation strategies, e.g., Kalman filtering, for estimating the direction and speed of wind based on SCADA, MET tower, or LiDAR measurements (see, e.g., [1]). However, the applicability of such approaches can be hindered by their reliance on computationally expensive models or costly sensing technologies. An alternative approach, would be to rely on the sequential self-correcting property of the Kalman filter in assimilating the predictions of reduced-order models of wind farm turbulence with measurements from inexpensive air-pressure sensors that are distributed across a wind farm.

Content from this work may be used under the terms of the Creative Commons Attribution 4.0 licence. Any further distribution of this work must maintain attribution to the author(s) and the title of the work, journal citation and DOI.

doi:10.1088/1742-6596/2767/5/052065

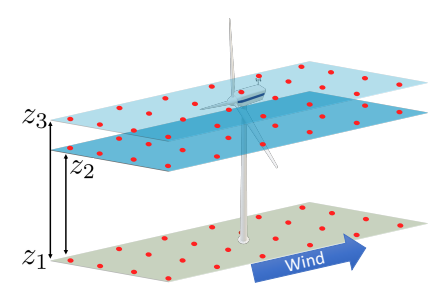


Figure 1. Two-point pressure correlations can be computed between points in measurement plane at or close to ground level $(y = z_1)$ and the model's computational planes $(y = z_2 \text{ or } z_3)$.

To achieve real-time estimation, the prior model used by the Kalman filter must be of low dimensional and dynamic complexity. A class of models that enables predictions of velocity fluctuations are given by the stochastically forced linearized Navier-Stokes (NS) equations [2, 3] around velocity profiles prescribed by engineering wake models, which typically cover a limited wall-normal range, e.g., a 2D plane at hub height [4, 5]. Accurate estimation also requires a reliable method for projecting field measurements from various locations throughout the wind farm to the model's computational domain. In our case, such measurements for Kalman filtering are provided by ground-level air-pressure sensors that are distributed across the farm. One solution to this problem is to utilize a data-driven inference technique such as linear stochastic estimation (LSE) to project ground pressure to the model's computational domain, which may be separated from the ground (e.g., at hub-height). The efficacy of such projection-based techniques, however, relies on strong two-point correlations of flow quantities between the measurement and computational domains (Fig. 1). In this paper, we first demonstrate how such two-point correlations are more pronounced for the pressure field relative to the velocity field and how they grow stronger as wall-normal separation reduces. Motivated by this finding, we then develop three-dimensional (3D) stochastic dynamical models of flow fluctuations that extend beyond the hub height and account for the vertical range affected by the rotor blades.

The remainder of the paper is organized as follows. In Sec. 2, we define the correlation metric used by our projection scheme and demonstrate the prevalence of two-point pressure correlations over the wall-normal dimension. In Sec. 3, we formulate the problem of how to model the 3D velocity fluctuation field around a static (mean) flow field provided by an engineering wake model. In Sec. 4, we provide details of the curled wake model we use to capture the long-time-averaged streamwise velocity around an operational wind turbine. In Sec. 5, we linearize the NS equations around the curled wake profile and devise a colored-in-time stochastic input that ensures statistical consistency between the linear model and a large-eddy simulation (LES). In Sec. 6, we demonstrate how our model completes the statistical signature of wind farm turbulence around an NREL-5MW wind turbine. Finally, we provide concluding remarks in Sec. 7.

2. Linear Stochastic Estimation

The existence of coherent motions in wall-bounded flows can result in strong two-point correlations of flow quantities, e.g., pressure and velocity, between points that are near the wall and points that are away from it [6]. Recently, near-wall pressure fluctuations have been shown to maintain higher levels of correlation with wall-separated regions up to the logarithmic region of the boundary layer [7]. This motivates the use of linear stochastic estimators for projecting ground measurements to wall-separated regions (and vice versa) using normalized variants of such two-point correlations [7]. Assuming a correlation between pressure within our model's computational domain $(p_{\rm m})$ and on the ground $(p_{\rm g})$, an estimate of the pressure in the ground-separated computational plane can be provided through the linear transformation

$$p_{\rm m}(x,z) = \mathcal{H}_{\rm mg}(x,z) p_{\rm g}(x,z). \tag{1}$$

doi:10.1088/1742-6596/2767/5/052065

Here, \mathcal{H}_{mg} is the normalized two-point correlation between two wall-parallel planes,

$$\mathcal{H}_{\mathrm{mg}}(x,z) := \frac{\langle p_{\mathrm{m}}(x,z) \, p_{\mathrm{g}}(x,z) \rangle}{\langle p_{\mathrm{g}}(x,z) \, p_{\mathrm{g}}(x,z) \rangle}$$

that is trained offline using a time-resolved pressure field resulting from high-fidelity simulations or field measurements. In this definition, $\langle \cdot \rangle$ is an expectation operator that is computed over a sufficiently long time window to ensure statistical convergence in \mathcal{H}_{mg} . Table 1 shows the normalized two-point correlations computed from LES-generated velocity and pressure fields [8]; see [4, Sec. 5.1] for details of the LES. As evident from this table, correlations of pressure are more pronounced than of velocity, which is in agreement with earlier studies of boundary layer flows [7], and their strength grows as the wall-normal separation reduces. This motivates the development of a 3D reduced-order model for velocity fluctuations that extends beyond hub height and accounts for the vertical range affected by the rotor blades.

Table 1. Normalized two-point correlations of velocity and pressure between a point on the ground that is 1 diameter in front of a turbine and points directly above it. Subscripts g, h, and m denote the ground, hub-height, and target locations, respectively, and $\langle \cdot \rangle$ is the expectation operator computed over a long time window.

$y/y_{ m h}$	1	0.86	0.71	0.57	0.43	0.29
$\overline{\langle u_{\rm g} u_{\rm m} \rangle / \langle u_{\rm g} u_{\rm g} \rangle}$	0.472	0.302	0.362	0.529	0.625	0.642
$\overline{\langle p_{ m g}p_{ m m} angle/\langle p_{ m g}p_{ m g} angle}$	0.776	0.880	0.986	0.994	0.995	0.998

3. Problem formulation

The static predictions of modern engineering wake models (e.g., [9]) constitute a basic flow profile around which fluctuations of the velocity field evolve. Based on this, the total wind velocity \mathbf{u} impinging a wind farm can be decomposed into the sum of a static base flow $\bar{\mathbf{u}}$ and dynamic velocity fluctuations \mathbf{v} , i.e.,

$$\mathbf{u}(\mathbf{x},t) = \bar{\mathbf{u}}(\mathbf{x}) + \mathbf{v}(\mathbf{x},t).$$

In this work, we provide a reduced-order model for the dynamics of fluctuations \mathbf{v} that can augment the predictions of the lower fidelity model of $\bar{\mathbf{u}}$ such that the overall model is statistically consistent with the result of high-fidelity simulations. To this end, we follow Bhatt et al. [4] in adopting a modeling framework that is based on the stochastically forced linear time-invariant (LTI) approximations of complex systems whose dynamics are represented by nonlinear partial differential equations [10, 11, 12, 13]. In this approach, the fluctuation field \mathbf{v} is assumed to be a zero-mean Gaussian process whose evolution is given by the LTI model with state-space representation

$$\mathbf{v}_t(\mathbf{x},t) = A\mathbf{v}(\mathbf{x},t) + B\mathbf{d}(\mathbf{x},t) \tag{2}$$

where \mathbf{v}_t is derivative of \mathbf{v} with respect to time t, $\mathbf{x} = (x, y, z)$ is the spatial coordinate, A is the generator of the linear dynamics, and B is an input matrix that introduces Gaussian process \mathbf{d} into the dynamics.

In Sec. 5, we show how the stochastically forced linearized NS equations can be used as a physics-based model for the evolution of fluctuations \mathbf{v} . We also show how the spectral content of \mathbf{d} can be determined to match a partially available set of second-order velocity correlations. The resulting dynamical model is of low complexity and thereby well suited for real-time estimation using conventional Kalman filtering algorithms. Moreover, due to the established statistical consistency with high-fidelity models, it also provides a solution to Kalman filtering in the presence of colored-in-time process noise with unknown dynamics [14]. We next provide details of recently developed engineering wake model for the base flow $\bar{\mathbf{u}}$ that accounts for the effects yaw misalignment (e.g., wake deflection).

doi:10.1088/1742-6596/2767/5/052065

4. Curled Wake Model

In this section, we summarize details of a 3D engineering wake model that we use as the base velocity $\bar{\mathbf{u}}$ in developing model (2). This curled wake model accounts for the effect of counter-rotating vortex pairs that lead to a spanwise asymmetry in the wake of active turbines, the influence of the ground, and the deflection of the wake due to the misalignment of the turbine rotors with respect to the wind direction; see [15] for additional details.

Consider a 3D domain around the turbine rotor with streamwise (x), wall-normal (y), and spanwise (z) dimensions. We assume a 3D base velocity $\bar{\mathbf{u}}$ with a streamwise component composed of a streamwise-invariant velocity profile U(y) and a spatially varying perturbation $u'(\mathbf{x})$, and wall-normal and spanwise components, which do not include streamwise varying perturbations, such that $\bar{\mathbf{u}} = [U + u', V, W]^T$. Perturbations on the wall-normal and spanwise components of $\bar{\mathbf{u}}$ are neglected due to their insignificant effects on wake deformation beyond the spanwise effects already captured by the streamwise-invariant components (U, V, and W) [15]. The invariant component of the streamwise velocity follows the power law $U(y) = U_h(y/y_h)^{\alpha}$, where y_h and U_h denote the hub height and the inlet velocity at hub height, and α is the shear exponent, which is chosen to be 0.2 for neutrally stable on-shore atmospheric conditions. On the other hand, the wall-normal and spanwise components, which are responsible for the distinctive kidney-shaped wake profile created by this analytical model, are defined as

$$V = \sum_{i=1}^{N} \frac{z_i \Gamma_i}{2\pi \left(y_i^2 + z_i^2\right)} \left(1 - e^{-\left(y_i^2 + z_i^2\right)/\sigma^2\right), \quad W = \sum_{i=1}^{N} \frac{y_i \Gamma_i}{2\pi \left(y_i^2 + z_i^2\right)} \left(1 - e^{-\left(y_i^2 + z_i^2\right)/\sigma^2\right)$$

to capture the combined influence of vortices shed by the yawed turbine rotor and a single wake vortex that captures the effect of the turbine's rotational motion. Here, N is the assumed number of discrete shed vortices, σ is the size of the vortex core, and Γ_i is the strength of each vortex, which is determined by its distance from the rotor center as

$$\Gamma_i = -\frac{16}{\pi} \Gamma \frac{r_i^2}{ND^2 \sqrt{1 - (2r_i/D)^2}}$$
(3)

ensuring a total circulation strength of $\Gamma = (\pi/8)\rho D U_{\infty} C_T \sin(\gamma) \cos^2(\gamma)$, with D as the rotor diameter, γ as the rotor yaw angle, ρ as the air density, and C_T as the thrust coefficient for the given velocity U_{∞} . Ground effects can be incorporated into the model by mirroring the shed vortices with respect to the ground. Figure 2 depicts how near-surface vorticity patterns differ with and without ground effects. The other contributor to cross-plane velocities (V and V) is the wake rotation, which consists of a tangential velocity distribution within the rotor-projected area and is modeled by a single vortex of circulation strength

$$\Gamma_{wr} = 2\pi \left(a - a^2\right) U_{\infty} D/\lambda$$

where a is the induction factor based on the thrust coefficient C_T and λ is the tip speed ratio. Following Ref. [15], the downstream evolution of the streamwise perturbation is given by

$$U\frac{\partial u'}{\partial x} + V\frac{\partial (U + u')}{\partial y} + W\frac{\partial u'}{\partial z} = \nu_{eff} \Delta u'$$
(4)

where ν_{eff} is the effective viscosity and Δ is the Laplacian. The effective viscosity ν_{eff} is assumed to be the sum of turbulent viscosity given by $\nu_T := l_m^2 |\mathrm{d}u/\mathrm{d}y|$ and a stabilizing viscosity $\nu_{Re} = (U_\infty D)/Re$. Here, Re is the Reynolds number, $l_m = \kappa y/(1 + \kappa z/\lambda)$ is the mixing length determined by the von Kármán constant $\kappa = 0.4$, and $\lambda = 15$ is the value of l_m in the free

doi:10.1088/1742-6596/2767/5/052065

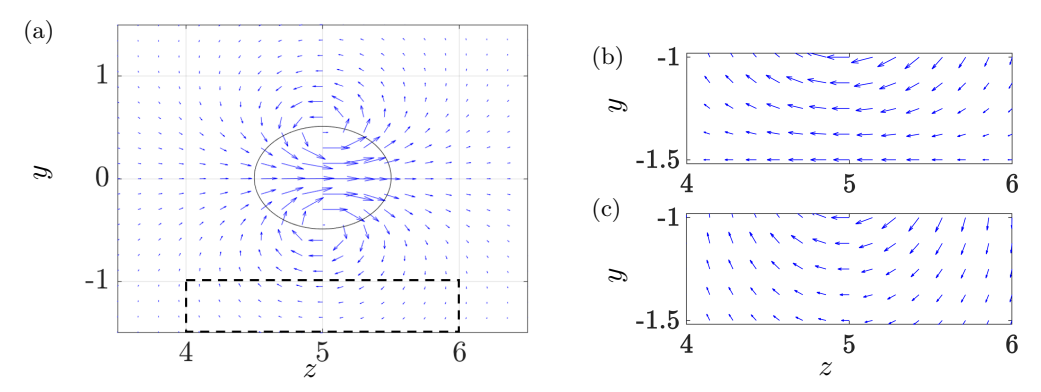


Figure 2. (a) Cumulative effect of vortices shed from a rotor plane (black circle) with $\gamma = 15^{\circ}$ yaw. Vorticies with (b) and without (c) ground effects from the rectangular region in (a).

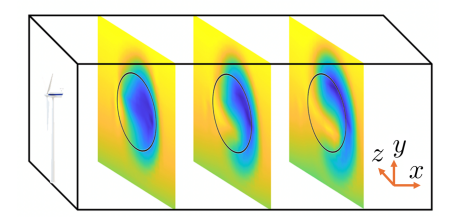


Figure 3. Streamwise evolution of the curled wake profile behind a turbine rotor with $\gamma = 15^{\circ}$ yaw. Black circles mark the rotor.

atmosphere [16, 17]. The solution u' to Eq. (4) can be obtained via spatial discretization in all three dimensions as the downwind march

$$u'_{[i+1,j,k]} = u'_{[i,j,k]} - \frac{\Delta x}{(U+u')_{[i,j,k]}} \left(V_{[i,j,k]} \frac{(U+u')_{[i,j+1,k]} - (U+u')_{[i,j-1,k]}}{\Delta y} + W_{[i,j,k]} \frac{u'_{[i,j,k+1]} - u'_{[i,j,k-1]}}{\Delta z} - \nu_{eff} \Delta u'_{[i,j,k]} \right).$$
(5)

At the cross-plane going through the rotor, we consider an initial perturbation velocity of $-2aU_{\infty}$ within the rotor-projected area that smooths out to zero (via a Gaussian smoothing scheme) at the edges. This represents the initial velocity deficit as the wind hits the rotor and its dissipation towards the lateral boundaries of the domain. This initial profile is then marched downstream using Eq. 5 to yield the curled velocity profile shown in Fig. 3. We note that in obtaining this profile, various numerical instabilities were identified and limited by enforcing a grid resolution of $\Delta x \leq 2\nu_{eff}U/V^2$ and $\Delta z \geq \sqrt{(2\nu_{eff}\Delta x)/U}$; see [15] for additional details.

5. Stochastic Dynamical Modeling of Wake Turbulence

In pursuit of a prior 3D reduced-order model for Kalman filtering, we follow the stochastic modeling framework of Zare et al. [12, 13] in capturing the dynamics of velocity fluctuations using the linearized NS equations. This approach has been previously employed in developing 2D models of hub-height turbulence that reproduce statistical signatures of multi-turbine wind farm flows in accordance with LES [4, 5]. We assume knowledge of a structured set of second-order statistics of wind farm flow. This information, together with an initial prediction of the wind velocity provided by an engineering wake model, such as the curled wake model described in the previous section, can be used to complete the statistical signature of the flow using an optimization-based method we summarize herein.

doi:10.1088/1742-6596/2767/5/052065

5.1. Stochastically Forced Linearized Navier-Stokes Equations

The dynamics of velocity \mathbf{v} and pressure p fluctuations around the base flow $\bar{\mathbf{u}}$ are governed by the linearized NS and continuity equations

$$\mathbf{v}_{t} = -(\nabla \cdot \bar{\mathbf{u}}) \mathbf{v} - (\nabla \cdot \mathbf{v}) \bar{\mathbf{u}} - \nabla p + \frac{1}{Re} \Delta \mathbf{v} - K^{-1} \mathbf{v} + \mathbf{d}$$

$$0 = \nabla \cdot \mathbf{v}$$
(6)

where $\mathbf{v} = [u, v, w]^T$ denotes the vector of velocity fluctuations, ∇ is the gradient operator, $Re = U_{\infty}D/\nu$ is the Reynolds number defined in terms of the velocity U_{∞} , rotor diameter D, and kinematic viscosity ν , and $\mathbf{d} = [d_u, d_v, d_w]^T$ is a zero-mean stationary stochastic input that triggers a statistical response of the linearized dynamics; see, e.g., [18, 13] for details on the formulation of the stochastically forced linearized equations. In obtaining these equations, length, velocity, time, and pressure have been non-dimensionalized by D, U_{∞} , D/U_{∞} , and ρU_{∞}^2 .

Equations (6) use a volume penalization technique to account for the effect of solid obstructions of the flow caused by turbine structures, e.g., turbine rotors, nacelles, and towers. This technique avoids the necessity for resolving the grid and implementing no-slide/no-penetration boundary conditions in complex geometries by reducing the velocity to zero in regions where $K^{-1} \to \infty$ and having no effect on the velocity elsewhere as $K^{-1} \to 0$ [19]. In this approach, the function $K(\mathbf{x})$ plays the role of a permeability function that captures the 3D turbine structure. To this end, we use the smooth 3D filter function

$$K^{-1}(\mathbf{x}) = \frac{m_K}{\pi^3} \left[\arctan\left(a_K(x - x_1)\right) - \arctan\left(a_K(x - x_2)\right) \right] \times$$

$$\left[\arctan\left(b_K(y - y_1)\right) - \arctan\left(b_K(y - y_2)\right) \right] \left[\arctan\left(c_K(z - z_1)\right) - \arctan\left(c_K(z - z_2)\right) \right]$$

where m_K determines the magnitude of the function, a_K , b_K , and c_K determine the slope of the function in various directions, and constants x_i , y_i , and z_i determine the spatial region over which the turbine structure affects the velocity field, with subscripts 1 and 2 corresponding to the start and end of this region, respectively. When accounting for the presence of yawed turbines, the coordinates and spatial limits $x_{1,2}$, $y_{1,2}$, and $z_{1,2}$ are rotated by the yaw angle. In practice, moderate values are assigned to the slope parameters as larger values can cause differentiability issues. On the other hand, our numerical experiments show that small values of m_k can result in spurious spikes in turbulence levels before turbine structures, while very large values can eliminate the velocity field. It is therefore important to tune this parameter to a sufficiently large value in order to ensure a satisfactory drop in the velocity field in regions that are influenced by the turbine structure. The colorplots in Fig. 4 show various views of a 3D resistance function $K^{-1}(\mathbf{x})$ used to generate the results in the next section.

A standard conversion for eliminating pressure [20] brings the linearized Eqs. (6) into the evolution form of Eq. (2) where A is a 3×3 operator valued matrix with blocks $A_{i,j}$ defined as

$$\begin{split} A_{11} \; &= \; \Delta^{-1} \left[\left(-U_{xyy} - U_{xzz} - K_{yy}^{-1} - K_{zz}^{-1} - (U_{yy} + U_{zz} + K_{x}^{-1}) \partial_x - (2U_{xy} + V_{yy} + V_{zz} + 2K_{y}^{-1}) \partial_y \right. \\ & - \left(2U_{xz} + W_{yy} + W_{zz} + 2K_{z}^{-1} \right) \partial_z - (U_x + K^{-1}) \partial_{xx} - 2U_y \partial_{xy} - (U_x + 2V_y + K^{-1}) \partial_{yy} \right. \\ & - 2U_z \partial_{xz} - 2(V_z + W_y) \partial_{yz} - (U_x + 2W_z + K^{-1}) \partial_{zz} - (U\partial_x + V\partial_y \Delta + W\partial_z) \, \Delta + (1/Re) \Delta^2 \right] \\ A_{12} \; &= \; \Delta^{-1} \left[-U_{yyy} - U_{yzz} - K_{xy}^{-1} + (K_y^{-1} + U_{xy} + V_{yy} + W_{yz}) \partial_x - 2U_{yy} \partial_y - 2U_{yz} \partial_z + U_y \partial_{xx} \right. \\ & + 2V_y \partial_{xy} + 2W_y \partial_{xz} - U_y (\partial_{yy} - \partial_{zz}) \right] \\ A_{13} \; &= \; \Delta^{-1} \left[-U_{yyz} - U_{zzz} + K_{xz}^{-1} + (U_{xz} + V_{yz} + W_{zz} + K_z^{-1}) \partial_x - 2U_{yz} \partial_y - 2U_{zz} \partial_z + U_z \partial_{xx} \right. \\ & + 2V_z \partial_{xy} + 2W_z \partial_{xz} - U_z (\partial_{yy} - \partial_{zz}) \right] \\ A_{21} \; &= \; \Delta^{-1} \left[U_{xxy} + K_{xy}^{-1} + 2U_{xy} \partial_x + (U_{xx} + K_x^{-1}) \partial_y + 2U_x \partial_{xy} \right] \\ A_{22} \; &= \; \Delta^{-1} \left[U_{xyy} - V_{yzz} + W_{yyz} - K_{xx}^{-1} - K_{zz}^{-1} + (-U_{xx} + U_{yy} - U_{zz} - 2K_x^{-1}) \partial_x + (U_{xy} - V_{zz} + W_{yz} - K_y^{-1}) \partial_y + (-2V_{yz} + W_{yy} - W_{zz} - 2K_z^{-1}) \partial_z + (-2U_x - V_y - K^{-1}) \partial_{xx} - 2U_z \partial_{xz} - 2V_z \partial_{yz} + (-V_y - K^{-1}) \partial_{yy} + (-V_y - 2W_z - K^{-1}) \partial_{zz} - U\partial_x \Delta - V\partial_y \Delta - W\partial_z \Delta + (1/Re) \Delta^2 \right] \end{split}$$

doi:10.1088/1742-6596/2767/5/052065

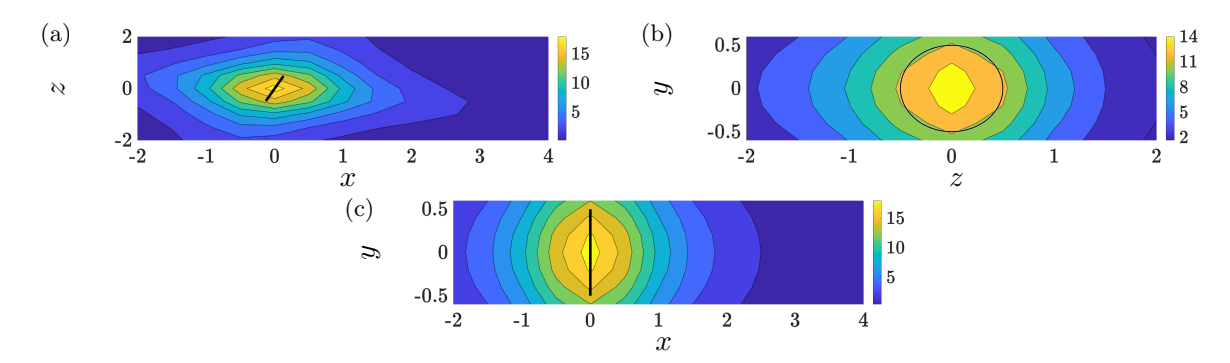


Figure 4. (a) Top; (b) front; and (c) side views of the resistance function $K^{-1}(\mathbf{x})$ (Eq. (7)) with $m_K = 10^6$, $a_K = b_K = c_K = 1$, $x_1 = -0.193$, $x_2 = 0.193$, $y_1 = -0.02$, $y_2 = 0.02$, $z_1 = -0.019$, $z_2 = 0.019$ rotated to correspond to a turbine with $\gamma = 15^{\circ}$ yaw. The top view is taken from hub height (y = 0), the front view is taken from the rotor plane (x = 0), and the side view is taken from z = 0. Black lines mark the turbine rotor.

$$\begin{split} A_{23} &= \Delta^{-1} \left[U_{xyz} - V_{zzz} + W_{yzz} + K_{yz}^{-1} + 2U_{yz}\partial_x + (U_{xz} + Vyz + W_{zz})\partial_y + (-2V_{zz} + 2W_{yz} + K_z^{-1})\partial_z - V_z\partial_{xx} + 2U_z\partial_{xy} + V_z\partial_{yy} + 2W_z\partial_{yz} - V_z\partial_{zz} \right] \\ A_{31} &= \Delta^{-1} \left[U_{xxz} + K_{xz}^{-1} + 2U_{xz}\partial_x + (U_{xx} + K_x^{-1})\partial_z + 2U_x\partial_{xz} \right] \\ A_{32} &= \Delta^{-1} \left[U_{xyz} + V_{yyz} - W_{yyy} + K_{yz}^{-1} + 2U_{yz}\partial_x + (2V_{yz} - 2W_{yy})\partial_y + (U_{xy} + V_{yy} + W_{yz} + K_y^{-1})\partial_z - W_y\partial_{xx} + 2U_y\partial_{xz} - W_y\partial_{yy} + 2V_y\partial_{yz} + W_y\partial_{zz} \right] \\ A_{33} &= \Delta^{-1} \left[U_{xzz} + V_{yzz} - W_{yyz} - K_{xx}^{-1} - K_{yy}^{-1} + (-U_{xx} - U_{yy} + U_{zz} - 2K_x^{-1})\partial_x + (-V_{yy} + V_{zz} - 2W_{yz} - 2K_y^{-1})\partial_y + (U_{xz} + V_{yz} - W_{yy} - K_z^{-1})\partial_z - (2U_x + W_z + K^{-1})\partial_{xx} - 2U_y\partial_{xy} - (2V_y + W_z + K^{-1})\partial_{yy} + 2W_y\partial_{yz} - (W_z + K^{-1})\partial_{zz} - (U\partial_x + V\partial_y + W\partial_z)\Delta + (1/Re)\Delta^2 \right] \end{split}$$

We use a finite difference method with extrapolated boundary conditions in the x-direction and Dirichlet and Neumann boundary conditions in the y and z directions (see [4, Appendix A] for details) to discretize the differential operators in the evolution model (2) and obtain

$$\dot{\mathbf{v}}(t) = A\mathbf{v}(t) + B\mathbf{d}(t) \tag{8}$$

where now $\mathbf{v}(t)$, $\mathbf{d}(t)$, A, and B are real-valued vectors and matrices of appropriate sizes. As mentioned earlier, the stochastic input \mathbf{d} provides a degree of freedom for shaping the statistics of the velocity field \mathbf{v} . Under steady atmospheric conditions, the linear dynamic system (8) is stable (A is Hurwitz). This means that if the pair (A, B) is controllable, persistent stochastic excitation of the linear dynamics yields the steady-state covariance matrix, i.e., $\mathbf{V} := \lim_{t \to \infty} \mathbf{E}[\mathbf{v}(t)\mathbf{v}^*(t)]$, that solves the Lyapunov-like equation

$$A\mathbf{V} + \mathbf{V}A^* = -BH^* - HB^*. \tag{9}$$

This equation relates the second-order statistics of \mathbf{v} to the spectral content of colored-in-time stochastic input \mathbf{d} provided by $H := \lim_{t \to \infty} \mathbf{E}[\mathbf{v}(t)\mathbf{d}^*(t)] + (1/2)B\Omega$. The entries of matrix \mathbf{V} in Eq. (9) represent two-point correlations of the velocity field at various spatial locations with diagonal entries denoting one-point correlations or the variance of \mathbf{v} and trace(\mathbf{V}) providing the total kinetic energy of the turbulent flow. In the special case of white state-independent input \mathbf{d} , $H = (1/2)B\Omega$ reducing Eq. (9) to the standard Lyapunov equation [12, Appendix B].

While white-in-time forcing is useful for analyzing the receptivity of the flow to external disturbances [18, 21], it is insufficient to account for statistical signatures computed from

doi:10.1088/1742-6596/2767/5/052065

experimental measurements or the result of numerical simulation [12, 5]. To address this issue, we employ an optimization-based framework for identifying the spectral content of colored-in-time forcing that reproduces and completes partially available second-order statistics of atmospheric turbulence in accordance with high-fidelity LES.

5.2. Identifying Colored-in-time Stochastic Input Via Covariance Completion

Given the dynamic generator A resulting from linearization of the NS equations and a set of available partial second-order statistics for the velocity field (i.e., velocity variances or intensities), we seek input matrix B and colored-in-time input \mathbf{d} that induce a statistical response from Eqs. (8) that reproduces the partially known statistical signatures of atmospheric turbulence around a wind turbine. To this end, we solve the covariance completion problem

minimize
$$-\log \det(\mathbf{V}) + \beta ||Z||_{\star}$$

subject to $A\mathbf{V} + \mathbf{V}A^* + Z = 0$
 $\mathbf{V}_{i,j} = G, \quad \forall \{i,j\} \in \mathcal{I}$ (10)

which minimizes a composite objective subject to two linear constraints. The first corresponds to the Lyapunov-like equation (Eq. 9) and the second constraint seeks to match known velocity variances from across the farm generated by a high-fidelity model. Matrices A and G are problem data, and Hermitian matrices \mathbf{V} and Z are optimization variables. The matrix G represents the partially available velocity statistics that correspond to entries of \mathbf{V} with indices from set \mathcal{I} . The objective function provides a trade-off between the solution to the maximum-entropy problem and the complexity of the forcing model, which we quantify as the number of degrees-of-freedom in the state-space of model (8) that are directly impacted by colored-in-time forcing \mathbf{d} . One way to penalize the latter is to regulate the number of independent columns of input matrix B, which can be bounded by the rank of matrix $Z := -BH^* - HB^*$. As the rank function is non-convex, problem (10) aims to penalize its convex proxy, i.e., the nuclear norm or sum of singular values of matrix Z, weighted by $\beta > 0$ against the logarithmic barrier function, which also ensures positive definiteness of the covariance matrix \mathbf{V} .

We solve convex optimization (10) using the customized algorithms developed in Ref. [11]. If the solution Z is sign-indefinite, the additive noise \mathbf{d} that generates the given steady-state statistics corresponding to set \mathcal{I} is colored-in-time. The coloring filter can be absorbed in the LTI dynamics (8) in a standard manner yielding the dynamically modified state-space representation

$$\dot{\mathbf{v}}(t) = (A - BK_f)\mathbf{v}(t) + B\mathbf{w}(t). \tag{11}$$

Here, **w** is white noise and matrix K_f is a parameter of the coloring filter with construction offered in [11, Sec. II.B].

6. Numerical Experiments

We provide a 3D stochastic dynamical model for the flow around a NREL-5MW reference wind turbine that is yawed $\gamma = 15^{\circ}$ against the wind. Following the LES that generated the training dataset [8], we consider the Reynolds number of the impinging flow to be $Re = 10^8$; see [4, Sec. 5.1] for LES details. When length-scales are normalized by the rotor diameter, the computational domain is given by $x \in [-2, 4]$, $y \in [-0.6, 0.6]$, and $z \in [-2, 2]$, with the turbine nacelle located at the origin $(y_h = 0)$. We use a uniform grid with $\Delta x = \Delta z = 0.5$ and $\Delta y = 0.1$, and a second-order central difference scheme to discretize the differential operators in the linearized equations. Grid convergence is ensured by doubling the number of discretization points. The curled wake profile we use as the base state for linearization considers $C_T = 0.7871$, a = 1/3, and $\lambda = 7.6$ corresponding to the maximum power from the NREL-5MW turbine. The LES-generated statistics fed into the optimization framework (Sec. 5.2) contain variances $\langle uu \rangle$,

doi:10.1088/1742-6596/2767/5/052065

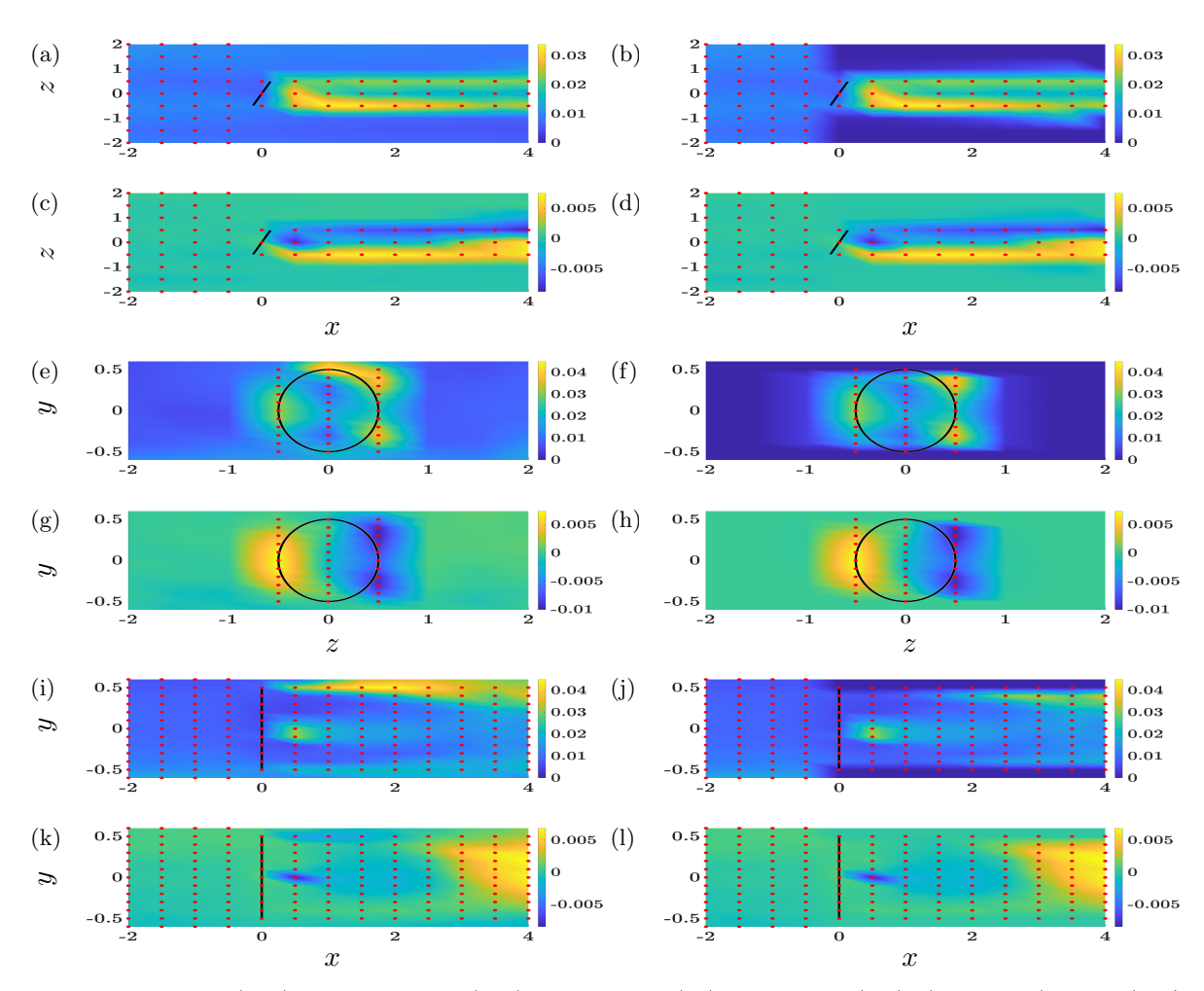


Figure 5. Top (a-d), cross-plane (e-h), and side (i-l) views of $\langle uu \rangle$ (a,b,e,f,i,l) and $\langle uw \rangle$ (c,d,g,h,k,l) resulting from LES (left column) and our stochastic model (right column) for a turbine yawed at 15°. The wind direction is from left to right. Top views taken from hub height, front views taken 3D downwind of the turbine, and side views taken from z=0. Red dots and black lines mark the training dataset and the rotor, respectively.

 $\langle vv \rangle$, and $\langle ww \rangle$ alongside $\langle uv \rangle$, $\langle uw \rangle$, and $\langle vw \rangle$. In the pursuit of a practical training scheme, we take these statistics from the inflow region upstream of the turbine and the space immediately behind its rotor throughout the domain (see red dots in Fig. 5).

Figure 5 compares the LES-generated streamwise variance $\langle uu \rangle$ and shear stress $\langle uw \rangle$ to the results of our stochastic model. The dominant features of the flow, such as high and low intensity regions, are well-captured, albeit there are spurious regions where the energy is underpredicted (Figs. 5(f) and 5(j)). The effects of tip vortices and the nacelle are also observed from the side views (Figs. 5(j) and 5(l)). While our model partly captures these effects, it struggles at the edges of the computational domain due to the lack of training data. We note, however, that in future work, such deficiencies may be overcome if the wall-normal extent of our computational grid is expanded. Other features, such as the wake asymmetry resulting from the turbine's rotation are also evident from the top and front views. Our results demonstrate the ability of our stochastic dynamical models in reproducing much of the statistical signature of the atmospheric turbulence surrounding this yawed turbine. The quality of completion in regions where LES data is not made available to the optimization framework is attributed to the Lyapunov-like constraint in

doi:10.1088/1742-6596/2767/5/052065

the covariance completion problem which allows the model to stay authentic to the flow physics (as captured by the linearized dynamics) while imposing consistency between the data and the linearized NS dynamics.

7. Conclusions

We extend prior developments on stochastic linear dynamical modeling of wind farm flows to 3D models that are well-suited for flow estimation based on ground pressure measurements. Such models are particularly useful in estimating wind farm flows that exhibit persistently strong correlations between the pressure on the ground and at hub height. Our models are based on the stochastically forced linearized NS equations around a curled wake profile that captures the effects of yaw misalignment on the downwind evolution of the wake. We employ a statistical modeling framework that enables the parameterization of colored-in-time process noise that ensures statistical consistency of our LTI models of velocity fluctuations with high-fidelity LES in matching normal and shear stresses of the wind. Our models are convenient for real-time data assimilation using conventional Kalman filtering algorithms due to their (i) physics-based nature, (ii) linearity, (iii) low computational complexity, and (iv) statistical consistency in matching important flow quantities. We particularly anticipate a desirable level of robustness to atmospheric variability due to their physics-based nature. Our ongoing efforts involve the identification of a minimal set of velocity correlations for training as well as the implementation of a Kalman-based wind forecasting tool built around such 3D models.

Acknowledgements

This work was supported in part by the National Science Foundation under awards 1916715 and 1916776 (I/UCRC for Wind Energy, Science, Technology, and Research) and from the members of WindSTAR I/UCRC. The presenting author is grateful to the Center for Wind Energy at UT Dallas for providing support for conference registration and travel.

References

- [1] Doekemeijer B M, Boersma S, Pao L Y, Knudsen T and van Wingerden J W 2018 Wind Energy Sci. 3 749–765
- [2] Jovanović M R 2021 Annu. Rev. Fluid Mech. 53 311-345
- [3] Abootorabi S and Zare A 2023 J. Fluid Mech. 958 A16 (32 pages)
- [4] Bhatt A H, Rodrigues M, Bernardoni F, Leonardi S and Zare A 2023 Energies 16 6908 (24 pages)
- [5] Rodrigues M, Burgess N A, Bhatt A H, Leonardi S and Zare A 2023 Robustness of two-dimensional stochastic dynamical wake models for yawed wind turbines Proceedings of the 2023 American Control Conference pp 818–823
- [6] Marusic I and Monty J P 2019 J. Fluid Mech. 51 49-74
- [7] Baars W J, Dacome G and Lee M 2023 arXiv preprint arXiv:2307.06449
- [8] Santoni C, Carrasquillo K, Arenas-Navarro I and Leonardi S 2017 Wind Energy 20 1927–1939
- [9] Bastankhah M and Porté-Agel F 2016 J. Fluid Mech. 806 506-541
- [10] Zare A, Jovanovic M R and Georgiou T T 2014 Completion of partially known turbulent flow statistics Proceedings of the 2014 American Control Conference pp 1680–1685
- [11] Zare A, Chen Y, Jovanovic M R and Georgiou T T 2017 IEEE Trans. Automat. Control 62 1368–1383
- [12] Zare A, Jovanovic M R and Georgiou T T 2017 J. Fluid Mech. 812 636-680
- [13] Zare A, Georgiou T T and Jovanovic M R 2020 Annu. Rev. Control Robot. Auton. Syst. 3 195–219
- [14] Zare A 2021 Data-enhanced kalman filtering of colored process noise *Proceedings of the 60th IEEE Conference* on Decision and Control pp 6603–6607
- [15] Martínez-Tossas L A, Annoni J, Fleming P A and Churchfield M J 2019 Wind Energy Science 4 127–138
- [16] Blackadar A 1962 J. Geophys. Res. 67 3095–3102
- [17] Sun J 2011 JAMC **50** 2030–2041
- [18] Jovanovic M R and Bamieh B 2005 J. Fluid Mech. **534** 145–183
- [19] Khadra K, Angot P and S Parneix J C 2000 Int J Numer Methods Fluids 34 651–684
- [20] Schmid P J and Henningson D S 2001 Stability and Transition in Shear Flows (New York: Springer-Verlag)
- [21] Ran W, Zare A, Hack M J P and Jovanovic M R 2019 Phys. Rev. Fluids 4 093901 (28 pages)